

Etching-Assisted Crumpled Graphene Wrapped Spiky Iron Oxide Particles for High-Performance Li-Ion Hybrid Supercapacitor

Eunji Kim, Hyeri Kim, Byung-Jun Park, Young-Hee Han, Jong Hyuk Park, Jinhan Cho, Sang-Soo Lee, and Jeong Gon Son*

From graphene oxide wrapped iron oxide particles with etching/reduction process, high-performance anode and cathode materials of lithium-ion hybrid supercapacitors are obtained in the same process with different etching conditions, which consist of partially etched crumpled graphene (CG) wrapped spiky iron oxide particles (CG@SF) for a battery-type anode, and fully etched CG for a capacitive-type cathode. The CG is formed along the shape of spikily etched particles, resulting in high specific surface area and electrical conductivity, thus the CG-based cathode exhibits remarkable capacitive performance of 210 F g^{-1} and excellent rate capabilities. The CG@SF can also be ideal anode materials owing to spiky and porous morphology of the particles and tightly attached crumpled graphene onto the spiky particles, which provides structural stability and low contact resistance during repetitive lithiation/delithiation processes. The CG@SF anode shows a particularly high capacitive performance of 1420 mAh g^{-1} after 270 cycles, continuously increases capacity beyond the 270th cycle, and also maintains a high capacity of 170 mAh g^{-1} at extremely high speeds of 100 C. The full-cell exhibits a higher energy density up to 121 Wh kg^{-1} and maintains high energy density of 60.1 Wh kg^{-1} at 18.0 kW kg^{-1} . This system could thus be a practical energy storage system to fill the gap between batteries and supercapacitors.

1. Introduction

With the increasing demand for large-scale energy storage systems, plug-in hybrid electric/electric vehicles, and small-scale wearable device fields, the energy storage devices should be improved to have much higher energy and power densities than conventional lithium-ion battery. Among various electrochemical energy storage systems including lithium-ion battery (LIB),^[1] supercapacitor,^[2,3] and lithium-ion hybrid supercapacitor (LIHS),^[4–7] the LIHS have become the focus of researchers for the higher energy density and the higher power density, which is composed of a capacitive-type electrode and a battery-type electrode. The LIHS would result in the higher energy density from the battery-type electrode and higher power density from the capacitive-type electrode. Conventional lithium-ion capacitors use carbon-based materials, such as lithium-doped graphite, as a negative

electrode and activated carbon as a positive electrode (as in conventional supercapacitors). Recently, several studies have focused on nanocarbon materials, including graphene and carbon nanotube (CNT)/battery-type nanocomposites, for higher energy storage performance in LIHS systems^[8–15] or LIB systems.^[16–19]


Graphene materials are especially promising candidates for energy storage electrodes. They have an extremely high theoretical surface area for a nanocarbon material ($\approx 2650 \text{ m}^2 \text{ g}^{-1}$), with remarkably high electrical conductivity, and high electrochemical and thermal stability.^[20–22] The most common method of manufacturing graphene on a large scale is to reduce graphene oxide (rGO) obtained from the chemical exfoliation of graphite (Hummer's method). However, rGO can be irreversibly aggregated and restacked during the reduction process, resulting in a significantly decreased surface area. To overcome rGO restacking, many studies have investigated nanostructure control of rGO, including crumpled morphology,^[23,24] graphene/CNT nanocomposites,^[25–27] and liquid-mediated nanostructuring.^[28] Our group also developed spikily dissolving

E. Kim, H. Kim, Dr. J. H. Park, Dr. S.-S. Lee, Dr. J. G. Son
Photo-Electronic Hybrids Research Center
Korea Institute of Science and Technology (KIST)
Seoul 02792, Republic of Korea
E-mail: jgson@kist.re.kr

E. Kim, Prof. J. Cho
Department of Chemical and Biological Engineering
Korea University
Seoul 02841, Republic of Korea

B.-J. Park, Dr. Y.-H. Han
Korea Electric Power Research Institute
Daejeon 34056, Republic of Korea

Dr. J. G. Son
Division of Energy and Environment Technology
KIST School
Korea University of Science and Technology (UST)
Seoul 02792, Republic of Korea

 The ORCID identification number(s) for the author(s) of this article can be found under <https://doi.org/10.1002/sml.201704209>.

DOI: 10.1002/sml.201704209

template-guided method for thoroughly crumpled nanostructures of rGO by etching GO-wrapped polycrystalline pseudo-cubic iron oxide microparticles.^[23] The crumpled graphene (CG) exhibits a larger specific surface area, a porous structure, high electrical conductivity, and antistacking property after pressurizing, which result in superior gravimetric and volumetric supercapacitor performance.

Besides, iron oxide, which we used template particles for fabricating crumpled graphene, is also known as anode material of lithium-ion battery.^[29,30] The iron oxide has many advantages for anode materials including a high theoretical capacity over 1000 mAh g⁻¹, low cost, nontoxicity, and high availability. As a representative form of iron oxide, the lithium storage mechanism of Fe₂O₃ is based on a redox conversion reaction between Li⁺ and Fe₂O₃, as can be described as Fe₂O₃ + 6Li⁺ + 6e⁻ ↔ 3Li₂O + 2Fe.^[17,29] This process usually causes a fast decrease in capacity, and suffers from poor cyclability due to severe volume changes during the charge/discharge cycle. Furthermore, the low conductivity of iron oxide inevitably reduces the rate capability of the electrode. To increase the Li storage capability of iron oxide, nanostructuring approach of iron oxide particles^[19,30–36] and nanocomposite approach with nanocarbon materials^[8–11,15–17,37–44] has been suggested and extensively studied. Nanostructured iron oxide can enhance the capacity and rate capability, due to the large surface area and fast Li⁺ diffusion paths. Nanocarbon composites can work as conductive additives with high surface areas to enhance electron transport of the less conductive iron oxide and elastic supports to improve the mechanical stability of the electrodes, and widely studied beyond the LIB field such as Li-S battery.^[45–47] Our partially etched, graphene wrapped spiky iron oxide polycrystalline particles^[23] can be an ideal anode materials for lithium-ion battery and lithium-ion hybrid supercapacitors, as they simultaneously encompass both spiked etched nanostructures and graphene-wrapped nanocomposite structures.

In this paper, we present a simple method of simultaneously obtaining a high-performance anode and cathode LIHS materials in one way from the GO-wrapped iron oxide particles, using partially etched and crumpled graphene-wrapped spiky iron oxide particles as a battery-type anode material and fully etched completely crumpled graphene as a capacitive-type cathode material. Crumpled graphene is chemically reduced and formed along the shape of a spikily etched particle, resulting in very high specific surface area and electrical conductivity, exhibiting remarkable capacitive performance of more than 210 F g⁻¹. The partially etched crumpled graphene-wrapped spiky iron oxide particles (CG@SF) are structurally stable and maintain extremely low resistance even during volume-changing lithiation/delithiation process because the spiky and porous dumbbell-shaped iron oxide particles closely adhere to crumpled graphene. The CG@SF anode exhibits very high capacitive performance of 1420 mAh g⁻¹ after 270 cycles and continuously increasing capacity beyond the 270th cycle and extremely high rate capability. The asymmetric full cell assembly of these two electrodes creates a LIHS with a higher energy density of 121 Wh kg⁻¹ and still high energy density of 60.1 Wh kg⁻¹ at an extremely high power density of 18.0 kW kg⁻¹ which values are some of the highest reported for LIHC materials.

2. Results and Discussion

Figure 1 shows the schematic images of template-guided formation of 3D crumpled graphene balls and graphene-wrapped spiky α -Fe₂O₃ particles for electrode materials of LIHSs. GO nanosheets formed via Hummers' method are generally negative charge ($Z \approx -25$ mV) due to the presence of hydroxyl and carboxyl functional groups. Polycrystalline α -Fe₂O₃ pseudo-cubic microparticles were prepared from ferric hydroxide gels by reacting NaOH with FeCl₃ and aging for 8 d. Their size are $\approx 1.2 \pm 0.1$ μ m. Synthesized α -Fe₂O₃ particles can be given a positive charge ($Z \approx +30$ mV) by treating with a polyethyleneimine (PEI) suspension. GO sheets successfully wrapped α -Fe₂O₃ particles due to the electrostatic interaction between negatively charged GO and positively charged PEI-treated α -Fe₂O₃ particles (GO@ α -Fe₂O₃, Figure 1a).

During the template-guided crumple structuring method, hydroiodic acid (HI) simultaneously acts as an etchant and a reducing agent. Hydrochloric acid (HCl) was used sequentially as a secondary etchant to control the etching rate of α -Fe₂O₃ particles. GO shells of GO@ α -Fe₂O₃ were reduced to rGO during HI treatment, increasing their hydrophobicity. Polycrystalline α -Fe₂O₃ was selectively etched in certain crystal planes, which changed their morphology from pseudocubic to dumbbell shapes with spikes like a sea urchin. Hydrophobically changed rGO shells continuously follow the spikily dissolving template particles due to hydrophobic interaction in an aqueous media. Thoroughly crumpled rGO was obtained after full etching of template particles. Figure 1b illustrates difference of the etched morphologies including pseudocubic, spiked iron oxide particles with rGO wrapping and fully etched CG, depending on the amount of HCl used. We used partially etched spiky rGO@ α -Fe₂O₃ nanocomposites for LIB-type anode materials, and fully etched highly crumpled rGO for supercapacitor-type cathode materials (Figure 1c).

Figure 2 shows morphological changes in rGO@ α -Fe₂O₃ nanocomposites etched with either 20, 30, 40, or 60 mL of a 35 wt% HCl aqueous solution. Figure 2a represents GO@pseudocubic α -Fe₂O₃ particles before the HI/HCl treatment. GO shells were successfully wrapped, and tightly adhered to pseudocubic α -Fe₂O₃ particles due to electrostatic interactions. During HI/HCl treatment, GO@ α -Fe₂O₃ particles were simultaneously reduced and etched, resulting in hydrophobic rGO sheets that continuously wrapped α -Fe₂O₃ particles (Figure 2b–d). After injecting 10 mL of a 10 wt% HI solution, and sequential addition of 20 mL of HCl (Figure 2b), α -Fe₂O₃ particles retained their pseudocubic shape while also forming a porous structure. As etching proceeded for 30 mL (Figure 2c) and 40 mL (Figure 2d) of HCl treatment, particles changed to a dumbbell shape with spikes such as a sea urchin. And the graphene continuously covers the particles along this spiky structure and forms highly crumpled morphology. The equivalent average size of spiky iron oxide particles was statistically measured to be 690 ± 80 nm. After fully etched condition (60 mL of HCl, Figure 2f), only highly crumpled rGO with porous structures were observed. We chose the 40 mL of HCl treated spiky etched α -Fe₂O₃ with crumpled rGO nanocomposites as an anode material because of the spikiest morphology with smaller size of iron oxide particles, which provide a larger surface area

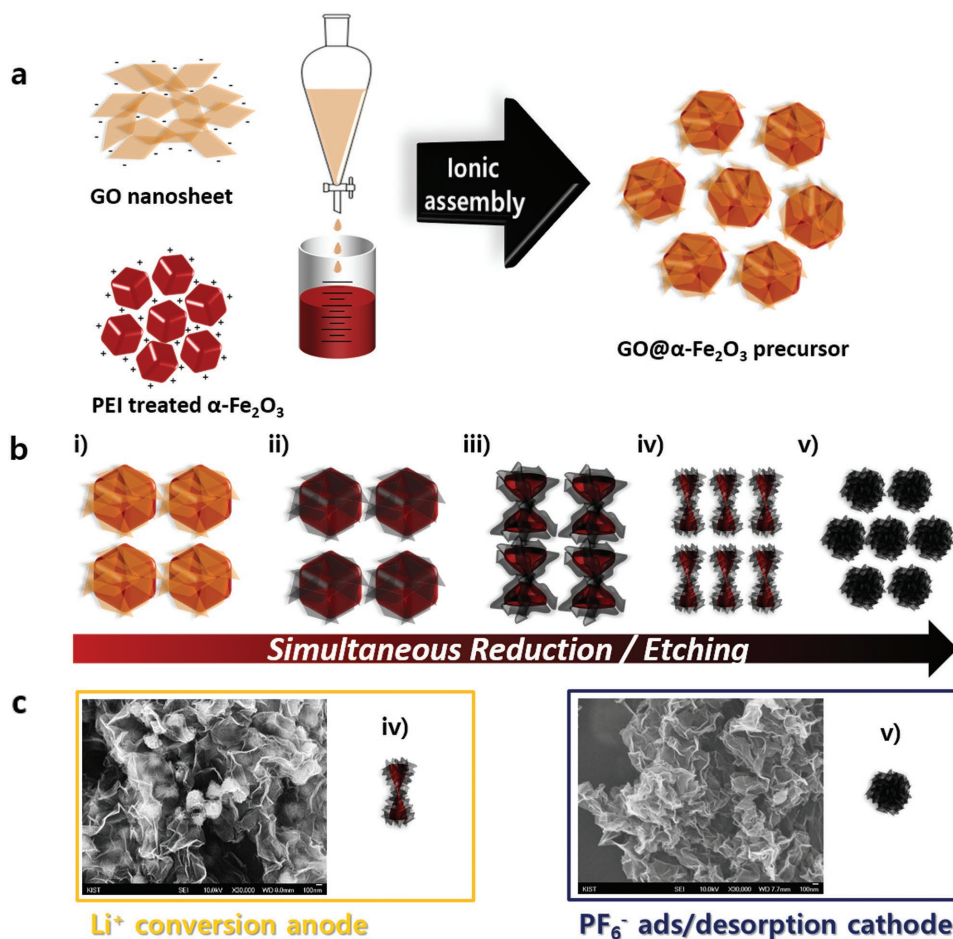


Figure 1. Schematic images of the template-guided formation of a crumpled graphene (CG) and crumpled graphene wrapped spiky iron oxide (CG@SF) for Li-ion hybrid supercapacitors. a) GO wrapped $\alpha\text{-Fe}_2\text{O}_3$ particles through the ionic assembly between negatively charged GO and positively charged PEI-treated $\alpha\text{-Fe}_2\text{O}_3$ particles. b) Under a HI/HCl treatment, the $\alpha\text{-Fe}_2\text{O}_3$ particles are gradually etched with spikes, while the GO are effectively reduced and follow the spikily dissolving particles and finally form highly crumpled morphology. c) Crumpled graphene wrapped spiky iron oxide (CG@SF) are used for conversion-type anode materials while fully etched highly CG are used for capacitive-type cathode materials.

for conversion reaction and facilitate electron transport with closely contacted crumpled graphene. The mass ratio of CG@SF is $\approx 1:9$ which can be obtained from comparing mass before and after the full etching process of the CG@SF.

The change in specific surface area of the GO@ $\alpha\text{-Fe}_2\text{O}_3$ and CG@SF composites or crumpled graphene according to etching condition was examined using nitrogen adsorption-desorption analysis and the Brunauer–Emmett–Teller (BET) method (Figure 3 and Table 1). Whereas the GO@ $\alpha\text{-Fe}_2\text{O}_3$ precursor showed relative low specific surface area of $20.3\text{ m}^2\text{ g}^{-1}$, partially etched CG@SF exhibited a significantly increased surface area of $169.5\text{ m}^2\text{ g}^{-1}$, and fully etched CG showed the largest surface area of $884.4\text{ m}^2\text{ g}^{-1}$. This resulted mainly from the nonporous structures of GO@ $\alpha\text{-Fe}_2\text{O}_3$, the porous structures of partially etched iron oxide, and crumpled graphene within CG@SF composites, and the thoroughly crumpled and macroporous structure of fully etched CG structures (without restacking). The increase in specific surface area and larger average pore diameter of the CG@SF composites means that spiky iron oxide particles provide more lithium storage sites and a larger contact area between the electrode and the electrolyte.

This results in faster Li^+ ion adsorption/desorption at the interface, which enhances specific capacity and rate capabilities.

The electrical conductivity of CG was obtained using a four-point probe method after the pressuring process. The density of the pressurized CG film is $\approx 0.7\text{ g cm}^{-3}$ and the measured electrical conductivity of CG film was $\approx 5000\text{ S m}^{-1}$ which is much higher value among the chemically reduced rGO. The rGO that results from HI reduction typically exhibits increased conductivity compared with other forms of chemically reduced rGO, including hydrazine or ascorbic acid.^[48] This high electrical conductivity of the CG can facilitate the charge carrier transport of the anode based on the CG itself and the cathode based on tightly adhered CG onto the poorly conductive $\alpha\text{-Fe}_2\text{O}_3$ particles.

To examine the capacitive-type performance of CG used as a cathode, we fabricated a CG//Li half-cell, as shown in Figure 4a. We used single-walled CNTs as a conductive additive and as a binder for the cell assembly. A dispersed solution of CG and CNTs were vacuum-filtered and pressed onto an Al current collector. The electrolyte consisted of 1 M of LiPF_6 in ethylene carbonate/diethyl carbonate/dimethyl carbonate (EC/DEC/DMC), with Li foil as a counter electrode. The cyclic

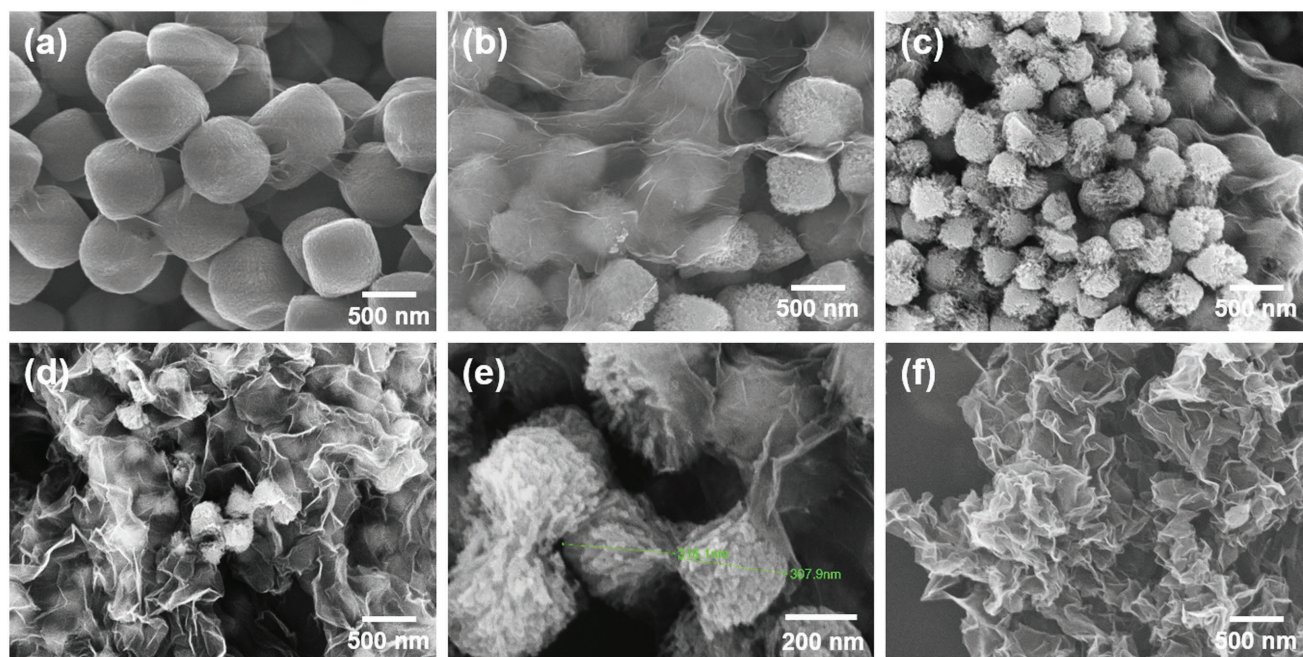


Figure 2. SEM images of a) graphene oxide wrapped iron oxide particles ($\text{GO}@ \alpha\text{-Fe}_2\text{O}_3$) before the HI treatment, partially etched crumpled graphene wrapped spiky $\alpha\text{-Fe}_2\text{O}_3$ ($\text{CG}@ \text{SF}$) after HI treatment with adding b) 20, c) 30, and d,e) 40 mL of HCl aqueous solution, and f) fully etched crumpled graphene (CG) after adding 60 mL of HCl.

voltammetry (CV) curve for the CG//Li electrode at a scan rate of 5 mV s^{-1} (Figure 4b) was rectangular shape with small pseudocapacitive peaks near 3.2 V, which indicate ideal electric double-layer capacitor (EDLC) behavior with small amount of pseudocapacitive property from the chemically reduced graphene. The galvanostatic charge/discharge (GCD) curves show nice triangle shape with few dynamic voltage (IR) drops

at current densities between 0.5 and 20 A g^{-1} (Figure 4c) in voltage window of $2.0\text{--}4.2 \text{ V}$ versus Li/Li^+ , where the of PF_6^- anion was physically adsorbed/desorbed at the CG porous surface. Figure 4d shows the specific capacitance obtained from GCD curves (ranging from 0.5 to 20 A g^{-1}). The specific capacitance of CG electrode is in the range from 212.3 to 189.0 F g^{-1} at current densities from 0.5 to 2 A g^{-1} , and 150.1 F g^{-1} even at the 20 A g^{-1} , demonstrating its excellent rate capabilities. Long-term stability was confirmed, as 91.4% of the capacitance was retained after 1000 cycles at 1 A g^{-1} (as shown in Figure 4e). High capacitive performance was due mainly to the high specific surface area of crumpled graphene, the relatively large pore sizes, and high electrical conductivity. Additionally, CNTs that acted as a conductive filler and binder also effectively grafted crumpled graphene, increasing their capacitive performance.

To evaluate the electrochemical lithium storage properties of the $\text{CG}@ \text{SF}$ anode, a $\text{CG}@ \text{SF}$ dispersed solution was mixed with CNT, vacuum-filtered and pressurized onto a Cu current collector in the same manner as used to assemble the cathode

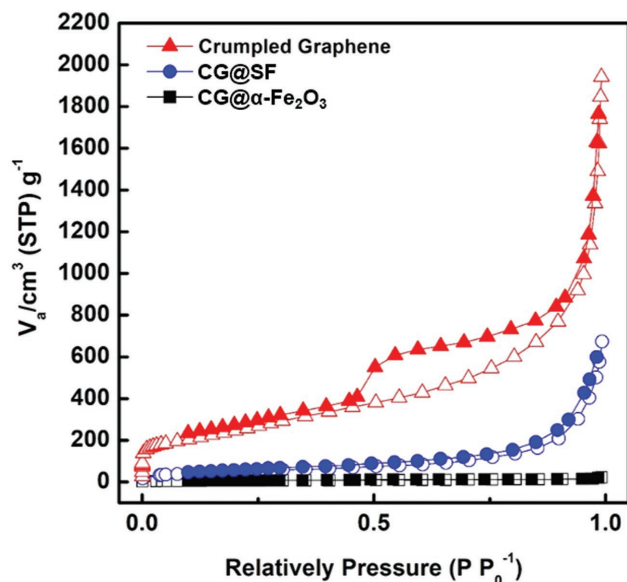


Figure 3. Nitrogen adsorption and desorption isotherm of $\text{GO}@ \alpha\text{-Fe}_2\text{O}_3$ particles, partially etched $\text{CG}@ \text{SF}$ particles, and fully etched crumpled graphene (CG).

Table 1. Specific surface area (SSA), total pore volume, and average pore diameter of graphene oxide wrapped iron oxide particles ($\text{GO}@ \alpha\text{-Fe}_2\text{O}_3$), crumpled graphene wrapped spiky iron oxide ($\text{CG}@ \text{SF}$), and fully etched crumpled graphene (CG) from the nitrogen adsorption and desorption experiment and a Brunauer–Emmett–Teller (BET) analysis.

	BET SSA [$\text{m}^2 \text{ g}^{-1}$]	Total pore volume [$\text{cm}^3 \text{ g}^{-1}$]	Pore diameter [nm]
$\text{GO}@ \alpha\text{-Fe}_2\text{O}_3$	20.294	0.03256	6.4182
$\text{CG}@ \text{SF}$	169.45	0.9788	23.106
CG	884.44	2.912	13.12

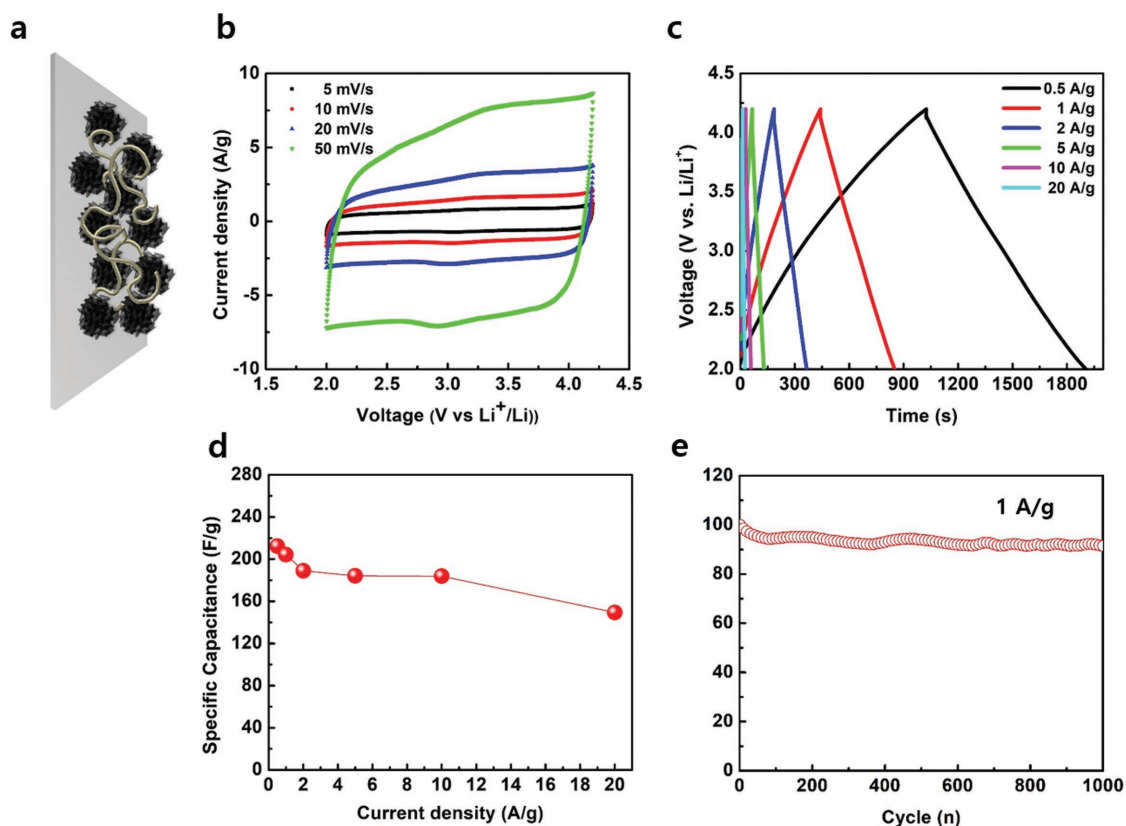
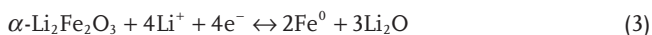
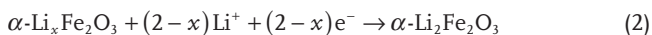
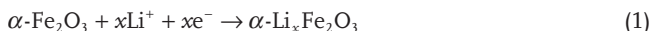


Figure 4. Electrochemical performances of the crumpled graphene (CG) electrode with a potential range of 2.0 and 4.2 V in 1 M LiPF₆ electrolyte. a) Schematic illustration of the CG with CNT electrode on an Al current collector. b) Cyclic voltammetry curves of half-cell device CG//Li at a scan rate from 5 to 50 mV s⁻¹ within 2.0–4.2 V versus Li/Li⁺ voltage window. c) Galvanostatic charge–discharge curves and d) specific capacitance of half-cell CG//Li at different current densities of 0.5–20 A g⁻¹ in the range of 2.0–4.2 V, and e) cycling performance test to 1000 cycles at 1 A g⁻¹.

electrode, as shown in **Figure 5a**. Figure 5b,c shows CV profiles at 0.5 mV s⁻¹, and charge–discharge curves of the CG@SF electrode at a current density of 1 A g⁻¹ within a voltage window of 0.05–3.0 V versus Li/Li⁺, respectively. The initial discharge capacity was 1375 mAh g⁻¹. The first cathodic polarization scan within CV curves and initial discharge curves showed a large peak, a voltage plateau at 0.5 V, and a small peak near 1.2 V. Only one voltage plateau/peak at 1.8 V was present in CV charge curves and anodic scans. Subsequent curves were highly reproducible, with a cathodic and anodic peak/plateau pair at ≈0.8 and 1.8 V for reversible conversion reactions. The second discharge capacity cycle was 920.5 mAh g⁻¹. These results correspond to multiple irreversible electrochemical reactions between α-Fe₂O₃ and Li⁺, as follows^[17]



An irreversible capacity loss of 34% may be mainly due to irreversible processes (1) and (2), and the additional formation of a solid electrolyte interface film and electrolyte decomposition. These processes commonly occur in most anode materials.

The X-ray diffraction (XRD) pattern in Figure S1 (Supporting Information) at the charged/discharged states of the electrode fully supports this mechanism. We also observed this reaction. During the early stages of long-term cycles, the CG@SF capacity gradually decreased until the 50th cycle (as shown in Figure 5d), increasing continuously up to 1445 mAh g⁻¹ during the 270th cycle, which is higher than the initial capacity (1375 mAh g⁻¹). The phenomenon of increasing capacity with cycles has been reported for several nanostructured metal oxide electrodes^[30] and is commonly observed for iron oxide particles with graphene or CNT.^[17,30,38,39] Furthermore, the plateau region in the discharge curve (0.8 V; Figure 5b) decreased gradually as the cycles progressed. During this time, the linear region became larger, greatly affecting the increase in capacity. This result can be attributed mainly to the gradual capacitive capacity increase due to Li⁺ ion adsorption or the pseudocapacitive characteristics at the interface between the crumpled graphene and lithiated iron oxide active nanocrystals at low potential window, while battery capacity at 0.8 V from the iron oxide particles gradually decreases.^[30]

To analyze the observed increase in capacity, scanning electron microscopy (SEM) and transmission electron microscopy (TEM) images of the CG@SF nanocomposite electrodes at charged state after 200 cycles were compared to pristine CG@SF (Figure 5e–h and Figure S1, Supporting Information). The pristine dumbbell shape spiky α-Fe₂O₃ (SF) shows 690 ± 80 nm

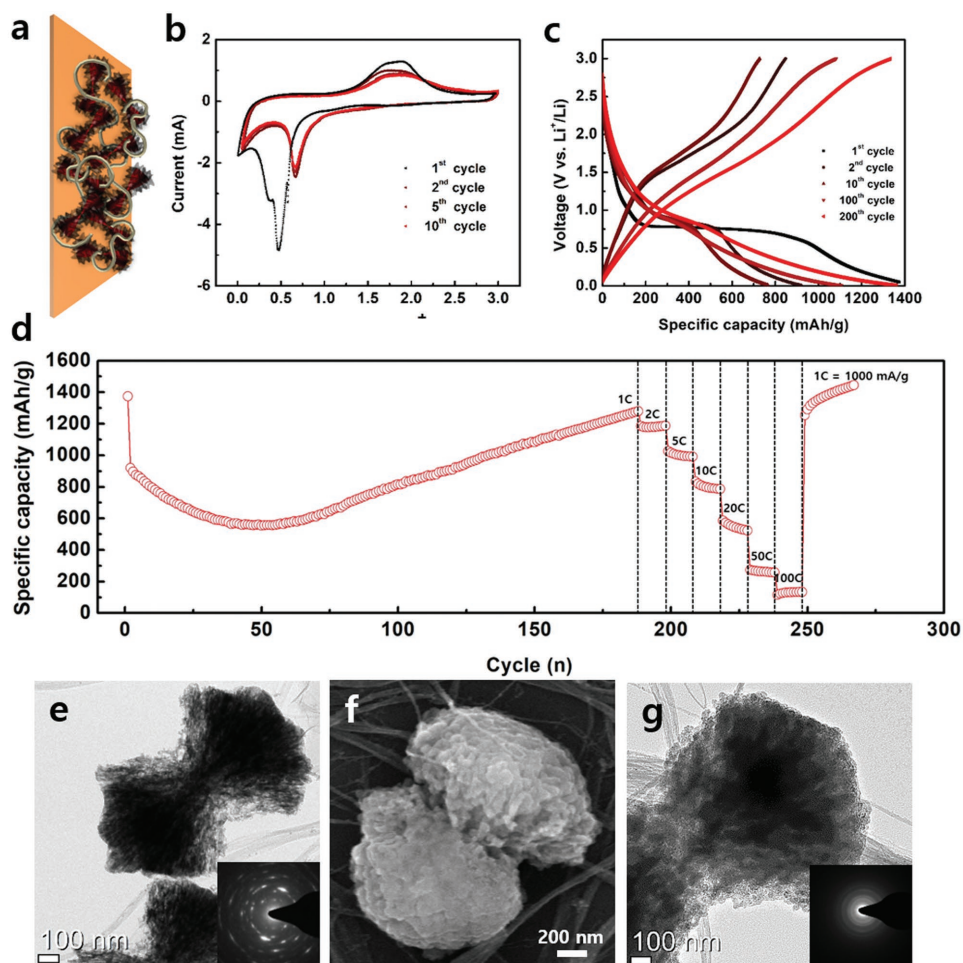


Figure 5. Electrochemical performances of the crumpled graphene wrapped spiky iron oxide (CG@SF) electrode with a potential range of 0.05–3.0 V in 1 M LiPF₆ electrolyte. a) Schematic illustration of the CG@SF electrode with CNT binders on a Cu current collector. b) CV curve of half-cell CG@SF//Li at a scan rate of 1 mV s⁻¹ with the different cycles in the voltage range of 0.05–3.0 V versus Li/Li⁺. c) Galvanostatic charge–discharge profiles of the CG@SF electrode at the current density of 1 C from the 1st to 200th cycles. d) Cycling performance of the CG@SF electrode at current density of 1 C to 200th cycles and consecutive rate capability test from 1 C to very rapid value of 100 C (1 C = 1000 mA g⁻¹). e) TEM images of pristine partially etched spiky α -Fe₂O₃ particles, f) SEM and g) TEM image of discharged state of CG@SF electrodes after 200 cycles.

of equivalent average size, with a porous and relatively large crystalline structure. This was confirmed using higher order peaks in selected area electron diffraction (SAED) patterns. After the 200th cycle, discharged particles still maintained their dumbbell shape and porous structure but the equivalent average size is 990 ± 120 nm, which is considerably larger than the pristine particles. The particles became less dense as their size increased; they became more porous and changed shape from a narrow bow-tie form to a fat, mushroom-like shape. This mainly originated from repetitive lithiation/delithiation reactions, which altered their volume. We noted several vague concentric rings in the SAED patterns and high-resolution TEM images (Figure S2, Supporting Information); this shows that nanosized small crystallites existed in the particles. Considering that the structural change of the particles steadily and stably occurs to a more porous and fat form during repetitive charging/discharging and plays a positive role, it can be seen that the CG@SF is suitable as an anode material of LIHC with long-term stability and high capacity.

In addition to the long-term cycling, the high-rate capability is also of great in considering the performance of LIHS systems. After 200 cycles, the CG@SF electrode was cycled at various C-rates from 1 to 100 C over a voltage range of 0.05–3.0 V versus Li/Li⁺, as shown in Figure 5b. The rate capability performance was excellent at capacities of 1280.5, 1184.5, 1026.9, 832.9, 585.7, 272.6, and 114.9 mAh g⁻¹ at 1, 2, 5, 10, 20, 50, and 100 C. After the deep rate performance test at 100 C, the cyclic test of CG@SF at the current density of 1 C was executed again. Surprisingly, we founded that the cycling performance of CG@SF was over 1400 mAh g⁻¹, which is even higher than before the rate capability test. This indicates that CG@SF electrodes within LIHS systems are excellent both in terms of long-term stability and rate capability performance.

Asymmetric LIHSs have a large operational voltage window; this contributes toward their high energy and power density potential within energy storage devices. We thus fabricated a hybrid supercapacitor using 4 V of voltage through low-potential reversible reactions between CG@SF anode electrodes and

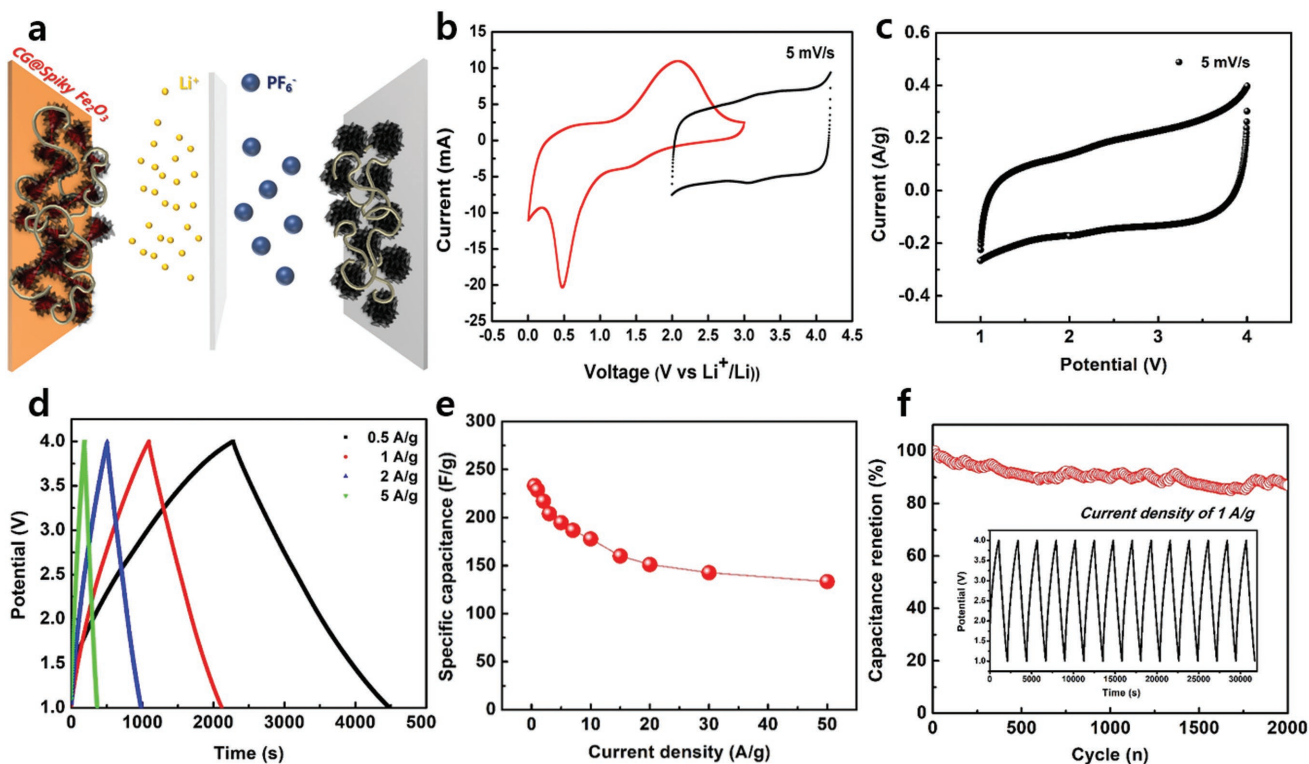


Figure 6. Electrochemical performances of the Li-ion hybrid supercapacitor (LIHC) in the CG@SF//CG full-cell configuration. a) Schematic illustration of the CG@SF//CG full-cell configuration. b) CV profiles of the operation potential range for the hybrid configuration and c) CV curve of hybrid full-cell device of CG@SF//CG at a scan rate at 5 mV s^{-1} in the voltage window of 1–4 V. d) Galvanostatic charge–discharge curves at different current densities from 0.5 to 50 A g^{-1} , e) specific capacitance and rate capability, and f) cycle stability of the CG@SF//CG hybrid full cell for 2000 cycles at a current density of 1 A g^{-1} .

capacitive CG cathodes, as shown in **Figure 6a**. The masses of the cathode and anode must be adjusted to match the capacity, due to the specific capacity difference between CG@SF and CG electrodes. We thus used an optimized mass ratio of 1:6.5 between the CG@SF and CG electrode. The CV curves of the half-cells (Figure 6b) with respective voltage windows versus Li/Li⁺ and the hybrid full-cell (Figure 6c) within a potential range from 1 to 4 V show relatively rectangular profiles for the electrochemical capacitor, indicating an interfacial reaction with a fast energy storage mechanism. We noted a pair of small peaks during the reversible lithiation/delithiation reaction of iron oxide active materials. GCD curves for the full cell showed a triangular shape, with a linear correlation between the ideal capacitor behavior and negligible IR drop; this could represent high electrical conductivity and very low resistance at the interface between the active materials (shown in Figure 6d). As shown in Figure 6e, the CG@SF//CG full cell exhibited an excellent capacitance of $\approx 238 \text{ F g}^{-1}$ at a current density of 0.2 A g^{-1} and a capacitance of $\approx 66\%$ even at a very high current of 50 A g^{-1} . This excellent rate capability and high capacitance is due mainly to the high electrical conductivity of the chemically reduced crumpled graphene, the structure of closely attached graphene to the spiky iron oxide particles, dumbbell shape spiky iron oxide particle itself, and the highly conductive CNTs that act as a conductive additive and a string-shape binder of particular CG or CG@SF active materials. Due to these structural specialties of two electrode materials, our hybrid supercapacitor cell can

exhibit excellent power density without significant decrease of the capacitance even under fast charging/discharging conditions over 50 A g^{-1} . This CG@SF//CG full cell also showed good cycle stability (Figure 6f) with the capacity retention of 87% after 2000 cycles with a high current density of 1 A g^{-1} .

Based on these performances of the hybrid system, we achieved a high energy density of 121 Wh kg^{-1} at 0.2 kW kg^{-1} and a 60.1 Wh kg^{-1} at a very high power density of 18.0 kW kg^{-1} (**Figure 7**). We compared the performance of our CG@SF//CG hybrid cell with that of reported Li-ion capacitors, as shown in a Ragone plot (Figure 7). While TiO_2 //graphene,^[49] $\text{Li}_4\text{Ti}_5\text{O}_{12}$ //graphene,^[50] $\text{Li}_4\text{Ti}_5\text{O}_{12}$ //3D graphene,^[51] MnO //graphene//N-doped carbon,^[9] Fe_3O_4 //graphene//3D graphene,^[10] and TiO_2 //graphene//activated carbon^[52] exhibited relatively high energy storage performance, our hybrid cells exhibited superior energy densities at extremely high power density due to their superior rate capability of individual electrodes. Additionally, LIB-level energy density was achieved with the hybrid cells, while maintaining supercapacitor-level power density, thus filling the gap between these two systems as an alternative system that combines the best performances of each.

3. Conclusion

In summary, we simply and simultaneously obtained anode and cathode materials of LIHCs in one way from the graphene

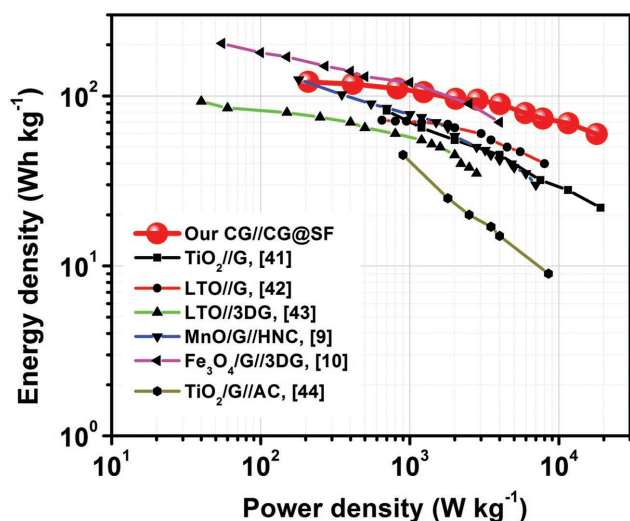


Figure 7. Ragone plots of the CG@SF//CG hybrid full cell compared with other reported graphene/CNT based hybrid-type capacitors.

oxide wrapped iron oxide particles depending on whether they are partially etched to form a crumpled graphene wrapped spiky iron oxide particles as an anode or completely etched to obtain a fully crumpled graphene as a cathode. The crumpled graphene is chemically reduced and formed along the spiky template shape, resulting in very high specific surface area and electrical conductivity, which was ideal for capacitive-type cathode materials. The CG@SF consisted of spiky and porous dumbbell-shaped iron oxide particles that adhered closely to the crumpled graphene. The CG@SF anode thus maintained structural stability and extremely low contact resistance, even during the lithiation/delithiation process. The CG@SF anode achieves considerably high capacity with increasing capacity over 270th cycles and extremely high rate capability. Through asymmetric assembly of these two electrodes, the Li-ion hybrid supercapacitors were fabricated and showed high energy density and much better power density compared to other systems, which could be another substantial energy storage system to fill the gap between the battery and supercapacitor. Our simultaneous manipulation of graphene and metal oxide structures can be used toward fabricating ideal electrode structures to improve the energy storage performance of materials beyond the lithium-ion hybrid capacitor, including LIB and next-generation secondary batteries.

4. Experimental Section

Materials: Ferric chloride hexahydrate ($\text{FeCl}_3 \cdot 6\text{H}_2\text{O}$, 99%), sodium hydroxide (NaOH, >97%), polyethylenimine (PEI, average $M_w \approx 25\text{k}$, branched), HI (57% by weight in 99.95% pure distilled water), and hydrochloric acid (HCl, 36.5–38.0%) were obtained from Sigma Aldrich Chemical Co. Single-walled carbon nanotubes (SWCNTs) were obtained from MEIJO Nano Carbon Co. (eDIPS).

Preparation of CG and CG@SF: To prepare polycrystalline $\alpha\text{-Fe}_2\text{O}_3$ pseudocubic microparticles, 1000 mL of a 5.4 M NaOH aqueous solution was added to a vigorously stirred solution of 1000 mL $\text{FeCl}_3 \cdot 6\text{H}_2\text{O}$ (2.0 M) in a 2000 mL glass bottle. This solution was stirred at room temperature for 30 min. Ferric hydroxide gels were aged at 100 °C for 8 d in a convection oven. Precipitates were washed several times with water

by centrifugation. GO was prepared from natural graphite according to a modified Hummers' method within ionic assembly and an etching/reduction process. $\text{GO}@-\text{Fe}_2\text{O}_3$ was formed via the electrostatic interaction between negatively charged GO and positively charged $\alpha\text{-Fe}_2\text{O}_3$ in an aqueous solution. To assemble GO layers onto $\alpha\text{-Fe}_2\text{O}_3$, a 0.1 wt% GO solution was slowly added to a 10 wt% PEI-coated $\alpha\text{-Fe}_2\text{O}_3$ suspension, and stirred at 300 rpm for 4 h. After this time, coagulated particles were purified through repeated centrifugation with deionized water to remove unassembled GO. Crumpled, graphene-wrapped, partially etched $\alpha\text{-Fe}_2\text{O}_3$ (CG@SF) nanocomposites were obtained from their $\text{GO}@-\text{Fe}_2\text{O}_3$ precursors using an HI reducing reagent and an HCl etchant used during the simultaneous etching/reduction process. Typically, 10 mL of HI solution was added dropwise into a vigorously stirred solution of 10 g of $\text{GO}@-\text{Fe}_2\text{O}_3$ within a dispersed aqueous suspension. After this, 40 mL of HCl was slowly added to the $\text{rGO}@-\text{Fe}_2\text{O}_3$ solution. To obtain crumpled rGO, 20 mL of the HCl solution was added during the HI and HCl treatment to fully etch $\alpha\text{-Fe}_2\text{O}_3$ particles. A reaction temperature of 90 °C was used for 8 h during the HI/HCl treatment. After the HI/HCl treatment, resulting CG@SF and CG were vacuum-filtrated and thoroughly washed with ethanol. CG@SF and CG powders were obtained by freeze-drying for several days.

LIHS Fabrication: CNT was dispersed in ethanol (1 mg/2 mL concentration) via a tip sonicator. 8 mg of CG@SF or CG and 4 mL of CNT dispersed in ethanol (with a CG:CNT and CG@SF:CNT mass ratio of 8:2) were mixed, to which 10 mL of ethanol was added. The vigorously mixed solution of CG/CNT and CG@SF/CNT in ethanol was vacuum-filtered and oven dried at 80 °C. CG/CNT and CG@SF/CNT electrodes were pressed on an Al foil for the CG/CNT electrode, and Cu foil for the CG@SF/CNT electrode. Both the capacitive-type electrode (CG), and the LIB-type electrode (CG@SF) were assembled using lithium metal foil for a counter electrode. This was done to fabricate the HS flat cell, and to measure the half-cell performance of each electrode. LIHS devices were assembled in the HS flat cell with an CG@SF anode and a CG cathode. All devices used 1 M LiPF_6 in a 1:1:1 (v/v/v) mixture of EC/DEC/DMC as an electrolyte; about 0.3–0.5 mL of electrolyte was used within each cell, and Celgard 3501 was used to separate the cells.

Characterization of Materials: Morphological characteristics were investigated using field-emission SEM (JSM-6701F, JEOL) and TEM (Tecnai F20, FEI). Structural characteristics were determined by film XRD (ATX-G, Rigaku). Nitrogen adsorption/desorption isotherms were determined at 77 K (Belsorp-MAX, SBEL Japan Inc.), and the specific surface area was calculated using the BET method. Sheet resistance was measured using a semi-automatic four-point probe (CRESBOX; Napson Inc., Japan).

Electrochemical Measurements: Electrochemical performance was measured by cyclic voltammetry. Galvanostatic charge/discharge measurements were made using a potentiostat/galvanostat instrument (PGSTAT-128N, Metrohm Autolab) and a multichannel potentiostat/galvanostat instrument (WMPG1000S, WonA Tech). The specific capacitance C_s (F g^{-1}) of the CG@SF//CG LIHS device was calculated as follows

$$C_s = \frac{4I}{m dV/dt} \quad (4)$$

where I is the current, m is the total mass of both electrodes, and dV/dt is the slope from the discharge curve (excepting the IR drop region). The energy density E (Wh kg^{-1}) and power density P (W kg^{-1}) of LIHCs were calculated using the following formula

$$E = \int_{t_1}^{t_2} IV dt \quad (5)$$

$$P = \frac{E}{\Delta t} \quad (6)$$

where V is the operating voltage, t_1 and t_2 are the start/end discharge times, and Δt is the discharge time. The CG@SF mass ratio (negative

electrode) and CG (positive electrode) within the CG@SF//CG LIHS setup was calculated using the following

$$Q^+ = Q^- (m^+q^+ = m^-q^-) \quad (7)$$

where Q and q indicate the capacity and specific capacity, respectively, and m is the mass of both electrode materials.

Supporting Information

Supporting Information is available from the Wiley Online Library or from the author.

Acknowledgements

The authors gratefully acknowledge financial support from the Global Frontier Research Program (2011-0032156) funded by the Korean Government (MEST), the R&D Convergence Program of NST (National Research Council of Science & Technology) of the Republic of Korea, and the Korea Institute of Science and Technology (KIST) internal project and internal project of Korea Electric Power Research Institute in Korea Electric Power Corporation. This work was also supported by the National Research Foundation (NRF) grant funded by the Ministry of Science, ICT & Future Planning (MSIP) (2015R1A2A1A10114354).

Conflict of Interest

The authors declare no conflict of interest.

Keywords

crumpled graphene, Li-ion hybrid supercapacitors, partially etched iron oxide, spiky iron oxide particles, supercapacitors

Received: December 3, 2017

Revised: January 24, 2018

Published online:

- [1] N. Nitta, F. Wu, J. T. Lee, G. Yushin, *Biochem. Pharmacol.* **2015**, *18*, 252.
- [2] J. R. Miller, P. Simon, *Science* **2008**, *321*, 651.
- [3] G. Wang, L. Zhang, J. Zhang, *Chem. Soc. Rev.* **2012**, *41*, 797.
- [4] D. P. Dubal, O. Ayyad, V. Ruiz, P. Gómez-Romero, *Chem. Soc. Rev.* **2015**, *44*, 1777.
- [5] G. G. Amatucci, F. Badway, A. Du Pasquier, T. Zheng, *J. Electrochem. Soc.* **2001**, *1488*, 930.
- [6] W. Zuo, R. Li, C. Zhou, Y. Li, J. Xia, J. Liu, *Adv. Sci.* **2017**, *4*, 1600539.
- [7] V. Aravindan, J. Gnanaraj, Y. Lee, S. Madhavi, *Chem. Rev.* **2014**, *114*, 11619.
- [8] Y. Ma, H. Chang, M. Zhang, Y. Chen, *Adv. Mater.* **2015**, *27*, 5296.
- [9] M. Yang, Y. Zhong, J. Ren, X. Zhou, J. Wei, Z. Zhou, *Adv. Energy Mater.* **2015**, *5*, 1500550.
- [10] F. Zhang, T. Zhang, X. Yang, L. Zhang, K. Leng, Y. Huang, Y. Chen, *Energy Environ. Sci.* **2013**, *6*, 1623.
- [11] K. H. Lee, Y.-W. Lee, S. W. Lee, J. S. Ha, S.-S. Lee, J. G. Son, *Sci. Rep.* **2015**, *5*, 13696.
- [12] K. Naoi, K. Kisu, E. Iwama, S. Nakashima, Y. Sakai, Y. Orikasa, P. Leone, N. Dupre, T. Brousse, P. Rozier, W. Naoi, P. Simon, *Energy Environ. Sci.* **2016**, *9*, 2143.
- [13] E. Iwama, N. Kawabata, N. Nishio, K. Kisu, J. Miyamoto, W. Naoi, P. Rozier, P. Simon, K. Naoi, *ACS Nano* **2016**, *10*, 5398.
- [14] E. Environ, K. Naoi, S. Ishimoto, J. Miyamoto, W. Naoi, *Energy Environ. Sci.* **2012**, *5*, 9363.
- [15] H. Kim, M. Cho, M. Kim, K. Park, H. Gwon, Y. Lee, K. C. Roh, K. Kang, *Adv. Energy Mater.* **2013**, *3*, 1500.
- [16] I. H. Son, J. H. Park, S. Park, K. Park, S. Han, J. Shin, S. Doo, Y. Hwang, H. Chang, J. W. Choi, *Nat. Commun.* **2017**, *8*, 1561.
- [17] Z. Wang, D. Luan, S. Madhavi, Y. Hud, X. W. (David) Lou, *Energy Environ. Sci.* **2012**, *5*, 5252.
- [18] A. Eftekhari, *ACS Sustainable Chem. Eng.* **2017**, *5*, 2799.
- [19] S. Goriparti, E. Miele, F. De Angelis, E. Di, R. Proietti, C. Capiglia, *J. Power Sources* **2014**, *257*, 421.
- [20] R. Raccichini, A. Varzi, S. Passerini, B. Scrosati, *Nat. Mater.* **2015**, *14*, 271.
- [21] Y. Huang, J. Liang, Y. Chen, *Small* **2012**, *8*, 1805.
- [22] V. Chabot, D. Higgins, A. Yu, X. Xiao, Z. Chen, J. Zhang, *Energy Environ. Sci.* **2014**, *7*, 1564.
- [23] J. Y. Lee, K.-H. Lee, Y. J. Kim, J. S. Ha, S.-S. Lee, J. G. Son, *Adv. Funct. Mater.* **2015**, *25*, 3606.
- [24] K. Lee, D. Kim, Y. Yoon, J. Yang, H. Yun, I.-K. You, H. Lee, *RSC Adv.* **2015**, *5*, 60914.
- [25] D. T. Pham, T. H. Lee, D. H. Luong, F. Yao, A. Ghosh, V. T. Le, T. H. Kim, B. Li, J. Chang, Y. H. Lee, *ACS Nano* **2015**, *9*, 2018.
- [26] B. S. Kim, K. Lee, S. Kang, S. Lee, J. B. Pyo, I. S. Choi, K. Char, J. H. Park, S. Lee, J. Lee, J. G. Son, *Nanoscale* **2017**, *9*, 13272.
- [27] K. Lee, Y. Yoon, Y. Cho, S. M. Lee, Y. Shin, H. Lee, H. Lee, *ACS Nano* **2016**, *10*, 6799.
- [28] X. Yang, C. Cheng, Y. Wang, L. Qiu, D. Li, *Science* **2013**, *341*, 534.
- [29] L. Zhang, H. B. Wu, X. W. (David) Lou, *Adv. Energy Mater.* **2014**, *4*, 1300958.
- [30] L. Tian, M. Zhang, C. Wu, Y. Wei, J. Zheng, L. Lin, J. Lu, K. Amine, Q. Zhuang, F. Pan, *ACS Appl. Mater. Interfaces* **2015**, *7*, 26284.
- [31] L. Yu, H. B. Wu, X. W. (David) Lou, *Acc. Chem. Res.* **2017**, *50*, 293.
- [32] L. Yu, H. Hu, H. B. Wu, X. W. (David) Lou, *Adv. Mater.* **2017**, *29*, 1604563.
- [33] G. Gao, L. Yu, H. B. Wu, X. Wen, D. Lou, *Small* **2013**, *9*, 1741.
- [34] B. Wang, J. S. Chen, H. B. Wu, Z. Wang, X. W. (David) Lou, *J. Am. Chem. Soc.* **2011**, *133*, 17146.
- [35] F. Ma, H. B. Wu, C. Xu, L. Zhen, X. W. (David) Lou, *Nanoscale* **2015**, *7*, 4411.
- [36] J. S. Chen, T. Zhu, X. H. Yang, H. G. Yang, X. W. (David) Lou, *J. Am. Chem. Soc.* **2010**, *132*, 13162.
- [37] G. W. Zhou, J. Wang, P. Gao, X. Yang, Y. S. He, X. Z. Liao, J. Yang, Z. F. Ma, *Ind. Eng. Chem. Res.* **2013**, *52*, 1197.
- [38] W. Wei, S. Yang, H. Zhou, I. Lieberwirth, X. Feng, K. Müllen, *Adv. Mater.* **2013**, *25*, 2909.
- [39] T. Jiang, F. Bu, X. Feng, I. Shakir, G. Hao, Y. Xu, *ACS Nano* **2017**, *11*, 5140.
- [40] Y. Zhang, Z. Gao, N. Song, X. Li, *Electrochim. Acta* **2016**, *222*, 1257.
- [41] Z. Gao, W. Yang, J. Wang, N. Song, X. Li, *Nano Energy* **2015**, *13*, 306.
- [42] Z. Gao, N. Song, X. Li, *J. Mater. Chem. A* **2015**, *3*, 14833.
- [43] Z. Gao, C. Bumgardner, N. Song, Y. Zhang, J. Li, X. Li, *Nat. Commun.* **2016**, *7*, 1.
- [44] Z. Gao, N. Song, Y. Zhang, X. Li, *RSC Adv.* **2015**, *5*, 15438.
- [45] Z. Gao, Y. Zhang, N. Song, X. Li, *Electrochim. Acta* **2017**, *246*, 507.
- [46] Y. Zhang, Z. Gao, X. Li, *Small* **2017**, *13*, 1.
- [47] Z. Gao, N. Song, Y. Zhang, X. Li, *Nano Lett.* **2015**, *15*, 8194.
- [48] I. K. Moon, J. Lee, R. S. Ruoff, H. Lee, *Nat. Commun.* **2010**, *1*, 73.
- [49] H. Wang, C. Guan, X. Wang, H. J. Fan, *Small* **2015**, *11*, 1470.
- [50] L. Ye, Q. Liang, Y. Lei, X. Yu, C. Han, W. Shen, Z.-H. Huang, F. Kang, Q.-H. Yang, *J. Power Sources* **2015**, *282*, 174.
- [51] K. Leng, F. Zhang, L. Zhang, T. Zhang, Y. Wu, Y. Lu, Y. Huang, Y. Chen, *Nano Res.* **2013**, *6*, 581.
- [52] H. Kim, M. Y. Cho, M. H. Kim, K. Y. Park, H. Gwon, Y. Lee, K. C. Roh, K. Kang, *Adv. Energy Mater.* **2013**, *3*, 1500.